ACS OMEGA

http://pubs.acs.org/journal/acsodf

Article

Theoretical Evaluation of Electrochemical Nitrate Reduction Reaction on Graphdiyne-Supported Transition Metal Single-Atom Catalysts

Fei Ai and Jike Wang*

Cite This: *ACS Omega* 2022, 7, 31309−31317

Read Online

ACCESS | Metrics & More | Article Recommendations | Supporting Information

ABSTRACT: The electrochemical reaction can be applied as a powerful method to eliminate the pollution of nitrate (NO_3^-) and as a feasible synthesis to enable the conversion of nitrate into ammonia (NH_3) at room temperature. Herein, density functional theory calculations are applied to comprehensively analyze the electrochemical nitrate reduction reaction (NO_3RR) on graphdiyne-supported transition metal single-atom catalysts (TM@GDY SACs) for the first time. It can be found that the vanadium-anchored graphdiyne (V@GDY) displays the lowest limiting potential of −0.63 V versus a reversible hydrogen electrode among the investigated systems in this work. Notably, the competing hydrogen evolution reaction is relatively restrained due to the comparatively weak adsorption of the H proton on the TM@GDY SACs. Moreover, higher energy intake is needed to overcome the energy barrier during the formation of byproducts (NO_2, NO, N_2O, and N_2) on V@GDY without applying extra electrode potential, showing the selectivity of NH_3 in the NO_3RR process. The ab initio molecular dynamics simulation denotes that the V@GDY possesses excellent structure stability at the temperature of 600 K without much distortion, compared with the initial shape, indicating the promise for synthesis. This study not only offers a feasible NO_3RR electrocatalyst but also paves the way for the development of the NO_3RR process.

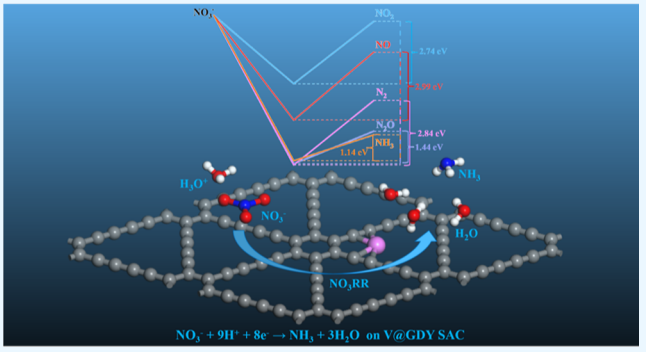

INTRODUCTION

Ammonia (NH_3) is a significantly important raw material in modern industrial production, which has been widely used in the chemical industry, light industry, chemical fertilizers, pharmaceutical, synthetic fiber, and other fields.[1,2] As early as the early 20th century, the emergence of the Haber-Bosch ammonia synthesis method solved the problem of the great demand for ammonia.[3,4] Nitrogen (N_2) and hydrogen (H_2) are the raw materials to synthesize the product NH_3 under extreme conditions (400−500 °C, 200−300 atm), which are both significantly energy-intensive and environment-malignant, responsible for ∼2% global annual energy consumption and ∼3% CO_2 global emission.[4−8] It seems to go against the concept of sustainable development from the view of environmental protection, so scientists are looking forward to finding new ammonia synthesis methods that can replace the Haber-Bosch method and meet the needs of industries.[9] Over the past few decades, the electrochemical nitrogen reduction reaction (NRR) seems to be a feasible method to produce NH_3 by reducing N_2.[10] Nevertheless, a lot of external energy is required to break the triple bond (941 kJ/mol) in the N_2 molecule to improve its reaction activity.[9,11] With the efforts of researchers and scientists, different kinds of efficient NRR electrocatalysts have already been produced to accelerate the NRR process.[12−14] However, a significant challenge of increasing the concentration of N_2 gas in the solution needs to be overcome due to a relatively high kinetic barrier occurring at the solid−liquid−gas interface in the NRR process.[15] Hence, the electrochemical synthesis of NH_3 using N_2 as a nitrogen source has a broad prospect, but there is still a long way to go to obtain considerable NH_3 yield in practical application.[16]

Nitrate (NO_3^-), one of the nitrogenous pollutants in wastewater, is an active compound that makes reaction easier than N_2 gas.[17] Domestic wastewater and residual chemical fertilizers, as well as untreated industrial wastewater, are the main source of NO_3^-. Applying electrochemical methods to degrade nitrogen-containing pollutants from industrial wastewater has become an important research field in environmental protection, intending to convert active nitrogen-containing species into N_2 gas instead of NH_3 gas.[18] Over the past few

Received: June 8, 2022
Accepted: August 15, 2022
Published: August 24, 2022

years, several metal catalysts and alloy catalysts have been developed to convert NO_3^- primarily into N_2 gas with excellent efficiency.[19,20] Hence, it will be a quite meaningful study to find new and efficient electrocatalysts for the selective conversion of NO_3^- into NH_3, which is rather beneficial both from the environmental perspective and from the economic perspective.

The single-atom catalysts (SACs) possess a large atomic utilization rate and highly active centers due to their unique configurations, which leads to excellent performance in various electrochemical reactions, such as the oxygen reduction reaction (ORR), hydrogen evolution reaction (HER), oxygen evolution reaction (OER), carbon dioxide reduction reaction (CO_2RR), and NRR.[21] The metal atoms in the SACs form a particular coordination configuration with the neighboring nonmetallic atoms on the substrate, whose structure often plays a significant role in the stability and activity of the SACs.[22] In other words, a special substrate needs the ability to trap the metal atoms stably to prevent the agglomeration of the adjacent metal atoms, which is fundamental for the high catalytic activity of the SACs. For instance, conventional porous two-dimensional materials can provide binding sites to anchor metal atoms to construct different kinds of SACs, such as metal oxides, graphene, and g-C_3N_4.[22,23]

Graphdiyne (GDY) is a rapidly rising star in the carbon family referring to a class of 2D carbon allotropes, whose theoretical model was first proposed by Haley in 1997, and the real structure was first synthesized experimentally in 2010.[24,25] The configuration of GDY is composed of the sp^2 hybrid benzene ring and sp hybrid diacetylene chain, which results in its unique chemical stability and mechanical stability.[26] Especially, GDY is a promising substrate for the SACs due to its natural uniform pores being conducive to the embedding of the metal atoms.[27] It is worth mentioning that many researchers have designed different kinds of graphdiyne-supported SACs with excellent catalytic performance experimentally and computationally. According to the theoretical calculation results, Ni@GDY,[28] Cu@GDY,[28] and Rh@GDY[29] display excellent electrocatalytic activity for the CO oxidation reaction. Pt@GDY,[30] Ni@GDY,[31] and Fe@GDY[31] have already been synthesized successfully, exhibiting desired electrocatalytic performance for the HER. In addition, Feng et al. have found that some TM@GDY SACs display a positive function in both the ORR and OER from the perspective of theoretical calculations.[32]

RESULTS AND DISCUSSION

Inspired by the above research results, a theoretical investigation of the electrochemical nitrate reduction reaction (NO_3RR) on the graphdiyne-supported transition metal SACs (TM@GDY SACs) (TM = Ti−Cu, Zr−Ag, Hf−Au) through first-principles calculation is expected to be conducted. First, the thermodynamic stability of the system consisting of the TM atoms and pristine GDY should be evaluated to determine which metal atoms possess the potential to form stable SACs with the pristine GDY. Subsequently, the electrocatalytic performance of all the thermodynamically-stable TM@GDY SACs in the process of reducing NO_3^- to NH_3 continues to be studied, and the origin of NO_3RR electrocatalytic performance for the most excellent TM@GDY SAC will be analyzed from the level of the electronic structure.

A 2 × 2 × 1 supercell of the pristine GDY monolayer is chosen to be optimized, whose optimized lattice constant reaches 9.454 Å, as shown in Figure 1a, which can be accepted with a negligible difference compared to the experiment

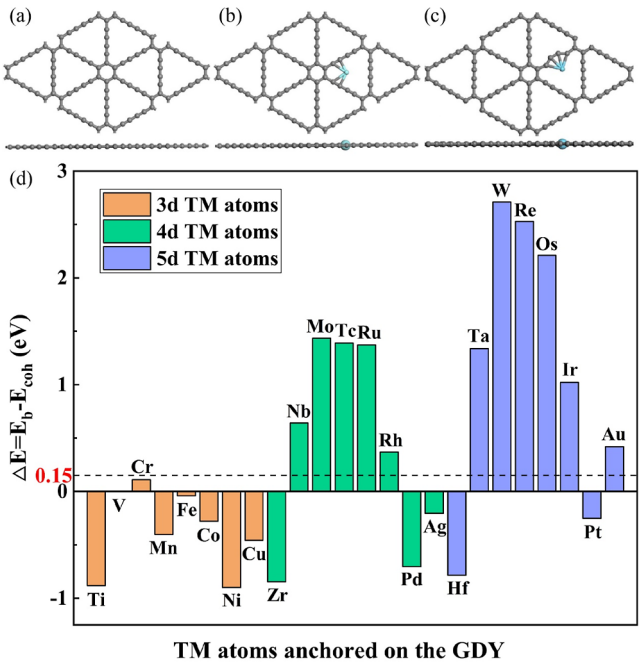

Figure 1. (a) Atomic structure of the pristine GDY monolayer with the view from the top and side. (b) Corner pattern and (c) center pattern structure of the TM@GDY SACs from the top view and side view. The gray and light blue balls represent the C and TM atoms, respectively. (d) Diagram of the energy difference (ΔE) between the binding energy (E_b) and cohesive energy (E_{coh}).

result.[26] Furthermore, 24 types of transition metals (Ti−Cu, Zr−Ag, Hf−Au) are chosen to be anchored on the pristine GDY, whose stability is evaluated by the energy difference between the binding energy (E_b) and cohesive energy (E_{coh}), as shown in Figure 1d. The optimized structures of all the TM@GDY SACs (TM = Ti−Cu, Zr−Ag, Hf−Au) can be divided into two species. The first configuration displays that the TM atoms are anchored at the corner of a triangular ring composed of 18 carbon atoms, called the corner pattern, as shown in Figure 1b, while the other configuration denotes that the TM atoms are anchored next to the center of the sp hybrid diacetylene chain, called the center pattern, as shown in Figure 1c. According to the analysis of the energy difference between the binding energy and cohesive energy and the criterion (ΔE < 0.15 eV), we can conclude that the ΔE values of the TM@GDY SACs (TM = Ti, V, Cr, Mn, Fe, Co, Ni, Cu, Zr, Pd, Ag, Hf, Pt) are less than 0.15 eV. Moreover, the details of the length of the TM-C bonds, binding energies, cohesive energies, and charge transfer are summarized in Table S1. These results are identical to previous studies,[33] proving the stability of the TM@GDY SACs (TM = Ti, V, Cr, Mn, Fe, Co, Ni, Cu, Zr, Pd, Ag, Hf, Pt) from the perspective of theoretical calculations.

The chemisorption of NO_3^- is the first step of the NO_3RR process, which plays an important role in the whole process. To evaluate how the chemisorption of NO_3^- affects the electrocatalytic reaction, it is necessary to calculate the adsorption strength of NO_3^- on the TM@GDY SACs (TM = Ti, V, Cr, Mn, Fe, Co, Ni, Cu, Zr, Pd, Ag, Hf, Pt). According to the previous studies,[34,35] there are two possible initial configurations adsorbed on the TM center called the 1-O

https://doi.org/10.1021/acsomega.2c03588
ACS Omega 2022, 7, 31309−31317

pattern (one oxygen atom adsorbed on the TM center of TM@GDY SACs) and the 2-O pattern (two oxygen atoms adsorbed on the TM center of TM@GDY SACs), as shown in Figure S1. With theoretical analysis of the data listed in Table S2, it can be found that the 2-O pattern exhibits more negative adsorption energies and more stable adsorbed configurations than the 1-O pattern. Therefore, it is reasonable to conclude that the 2-O pattern is the major configuration for NO_3^- adsorbed on the TM@GDY SACs. Moreover, the adsorption strength of NO_3^- on the pristine GDY monolayer is investigated as well with a value of +1.87 eV, proving the catalytic activation of the TM center in the TM@GDY SACs from another aspect. Notably, there are other competitive reactions against the NO_3RR, such as the HER and NRR. For a parallel comparison, the adsorption energies of NO_3^- (ΔG_{*NO_3}), H proton (ΔG_{*H}), and N_2 molecule (ΔG_{*N2}) on the TM@GDY SACs are shown in Figure 2a and Table S3,

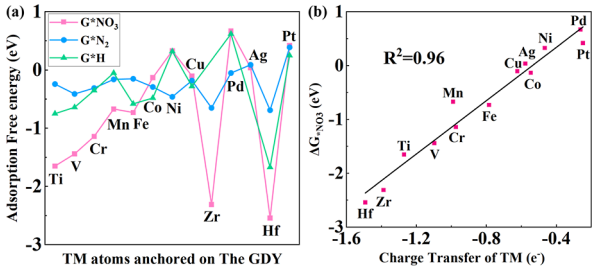

Figure 2. (a) Diagram of adsorption energies of NO_3^-, N_2 molecule, and H proton on the TM@GDY SACs for parallel comparison. (b) Scaling relation between charge transfer of the TM atoms and NO_3^- adsorption energies.

and the corresponding configurations of *H and *N_2 (* denotes the TM center) can be found in Figure S2. It can be inferred that ΔG_{*NO_3} values are more negative than ΔG_{*H} values, except Co@GDY and Cu@GDY with slightly more positive values, indicating that the NO_3RR is a more favorable competitor with the HER. Moreover, ΔG_{*NO_3} values even display a lower tendency than ΔG_{*N2} values for the early 3d TM@GDY SACs, which suggests that they may become superior candidates with higher selectivity of the NO_3RR toward NH_3 than that of the NRR.

To gain a deeper insight into the adsorption trends of NO_3^- on the TM@GDY SACs, the relationship between charge transfer of the TM atoms and ΔG_{*NO_3} values is shown in Figure 2b. They show a highly linear correlation with a nice correlation coefficient (R^2 = 0.96), which provides an appropriate explanation for the variation of NO_3^- adsorption; that is, to say, the TM center with a larger electron loss could contribute to stronger adsorption of NO_3^-. Taking Hf@GDY as an example, its adsorption is the strongest one with a negative value of −2.54 eV, resulting from the Hf atom with the largest charge transfer of 1.49 e^-, as listed in Table S1. Moreover, the positively charged TM atoms are easy for intermediates to be adsorbed, which can accelerate the subsequent reaction of the NO_3RR.

The NO_3RR is a reaction with complicated mechanisms, involving eight electrons participating in the whole steps.[36] Hence, there are different kinds of byproducts (NO_2, NO, N_2O, and N_2) potentially produced during the conversion process of NO_3^- to NH_3. Nevertheless, NH_3/NH_4^+ is the most thermodynamically stable product at negative electrode potential. According to the previous studies, receivable mechanisms for the NO_3RR process have already been proposed by Wang et al.,[34] indicating that four different configurations of adsorption intermediate *NO (called O-end, N-end, NO-side, and NO-dimer) might exist in the NO_3RR process, as shown in Figure S3, which results in four different types of the mechanisms of NO_3^- to NH_3 and a pathway from NO_3^- to N_2, as shown in Figure 3a. To simplify the computation and pick up the most suitable pathway, the adsorption energies of NO with different configurations were calculated. Based on the analysis of adsorption energy differences of these NO configurations, the N-end adsorption configuration was proved to be the most stable one. Legitimately, the N-end pathway mechanism was chosen as the most reasonable mechanism for the NO_3RR process. So the N-end pathway is mainly discussed in this study, in which each elementary step involved is displayed in the Supporting Information, while other pathways are not further studied.

The limiting potential (U_L), defined as $U_L = -\Delta G_{max}/e$, where ΔG_{max} denotes the maximum of free energy changes among all the elementary steps in the N-end pathway, is used to examine the NO_3RR performance on the TM@GDY SACs (TM = Ti, V, Cr, Mn, Fe, Co, Ni, Cu, Zr, Pd, Ag, Hf, Pt). The detailed free energy change values of each elementary step can be found in Tables S4 and S5. Moreover, it can be inferred from Figure 3b that the U_L values of the vanadium-anchored graphdiyne (V@GDY) and Ag@GDY are −0.63 and −0.65 V respectively, which are the lowest two among all the TM@GDY SACs, implying that they may be promising electrocatalysts for the NO_3RR to produce NH_3. Nevertheless, the U_L values of the TM@GDY SACs (TM = Ti, Zr, Pd, Hf, Pt) are not presented in Figure 3b, which can be attributed to the fact that some adsorption intermediates are unable to be adsorbed effectively on the TM center. Specifically speaking, for adsorption structures of all the five TM@GDY SACs (TM = Ti, Zr, Pd, Hf, Pt) shown in Figure S4, the *NO_3H intermediate displays an inactive connection with the TM center for Pd@GDY and Pt@GDY (Figure S4e,g), and an unstable connection with the TM center for Ti@GDY, Zr@GDY, and Hf@GDY (Figure S4a−c) after structure relaxation. Furthermore, for Pd@GDY and Pt@GDY, it is also difficult for the *NO_2H intermediate to be adsorbed on the TM center (Figure S4d,f). Notably, the *NO_3H intermediate turns into two parts consisting of *O and *NO_2H after structure relaxation for adsorption on the Ti@GDY, Zr@GDY, and Hf@GDY, while it remains a complete adsorption intermediate after structure relaxation without being adsorbed on the TM center of Pd@GDY and Pt@GDY, respectively. Inferentially speaking, the early transition metal atoms (Ti, Zr, and Hf) anchored on the GDY may lead to the high activity of the TM@GDY SACs, with the instability of the *NO_3H intermediate, leading to the splitting of the *NO_3H intermediate after optimization. On the contrary, the late transition metal atoms (Pd and Pt) embedded in the GDY exhibit more negative activity with the adsorption intermediates (*NO_2H and *NO_3H), leading to the desorption of *NO_2H and *NO_3H to the TM center.

As plotted in Figure 4a, the free energy diagram of the NO_3RR on V@GDY is further and mainly analyzed to validate the nitrate-to-ammonia performance, while the result of Ag@GDY is displayed in Figure S6 and not discussed in detail, whose thermodynamic stability is verified by the ab initio

https://doi.org/10.1021/acsomega.2c03588
ACS Omega 2022, 7, 31309−31317

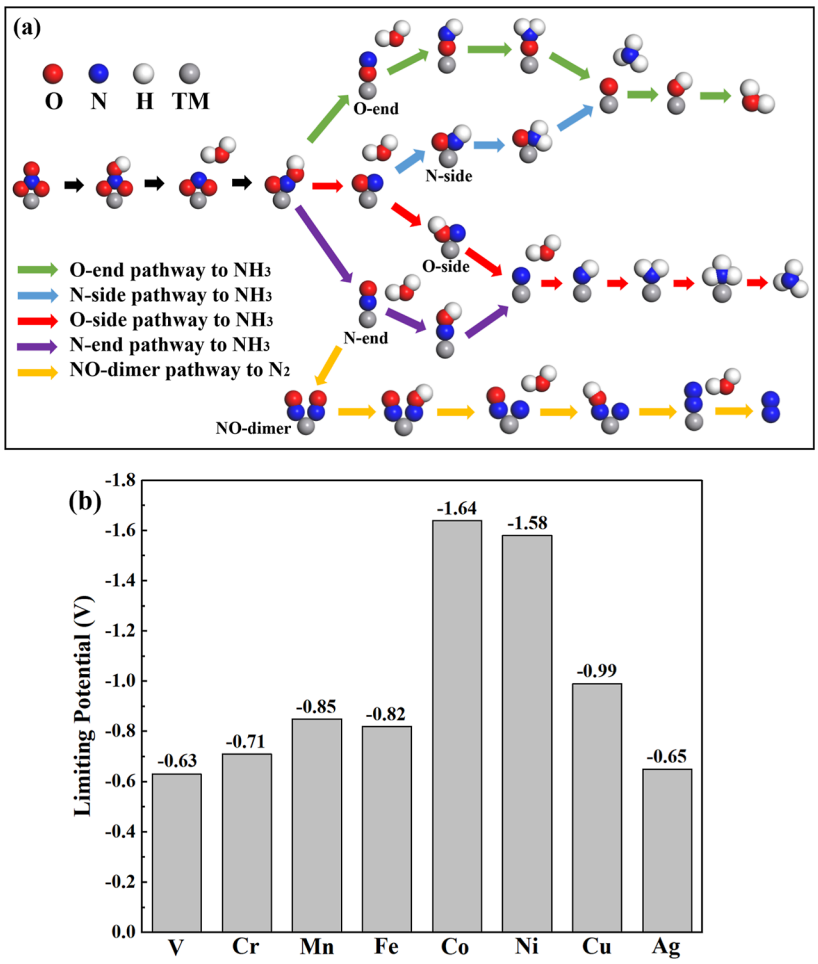

Figure 3. (a) Schematic diagram for detailed pathways of the NO_3RR, including O-end, O-side, N-end, and N-side pathway to NH_3 and the NO-dimer pathway to N_2. (b) Summary of limiting potentials on the TM@GDY SACs (TM = V, Cr, Mn, Fe, Co, Ni, Cu, Ag) for the NO_3RR via the most favorable N-end pathway.

molecular dynamics (AIMD) simulations shown in Figure S10. The corresponding structures of NO_3RR intermediates are shown in Figure 4b (via the N-end pathway) and Figure S7 (via the NO-dimer pathway). Moreover, the free energy diagrams of the NO_3RR (via the N-end pathway) on the other TM@GDY SACs (TM = Cr, Mn, Fe, Co, Ni, Cu) are also given in Figure S5,6, for comparison. It can be inferred that NO_3^- can be stably adsorbed with two TM-O bonds for the first step with an energy change of −1.44 eV. However, considering that the V atom is a little bit far away from the GDY plane displayed in Figure 4b, the AIMD simulation is carried out to check out the system stability of the structure of NO_3 adsorbed on V@GDY with the results displayed in Figure S11. Therefore, it is reasonably believable that the system of all kinds of intermediates adsorbed on V@GDY in the NO_3RR process is stable. Then, the following steps can be divided into two parts, with the seventh step used as the boundary. In the former part (from the second step to the seventh step), all the $*NO_x$ intermediates (x = 3, 2, 1) suffer an entirely endothermal process by the attack of the $(H^+ + e^-)$ pair to form their hydrogenated products, named $*NO_xH$ intermediates, with the energy change of +0.29, +0.27, and +0.63 eV, respectively. However, the corresponding $*NO_xH$ intermediates (x = 3, 2, 1) then go through an exothermal process with the release of H_2O, whose energies drop by 1.86, 1.87, and 1.37 eV, respectively. Afterward, the removal of an oxygen atom in $*NO_xH$ species (x = 3, 2, 1) requires the attack of the $(H^+ + e^-)$ pair two times, in which extra energy is needed to keep the elementary reaction on for the first attack, while with the energy release for the second attack. Subsequently, in the latter part (from the eighth step to the eleventh step), the *N intermediate is hydrogenated by the $(H^+ + e^-)$ pair consecutively three times to impel the formation of $*NH_3$ and the desorption of NH_3 eventually, with the energy changes of −0.67 eV for the step of *N to *NH, −0.41 eV for the step of *NH to $*NH_2$, 0.03 eV for the step of $*NH_2$ to $*NH_3$, and 1.14 eV for the desorption of NH_3, respectively. The tendency of the energy changes from the *N intermediate to the $*NH_2$ intermediate is downhill, while is uphill for the $*NH_2$ intermediate to the $*NH_3$ intermediate with an energy change nearly close to 0.00 eV (0.03 eV), implying the spontaneousness of the elementary reaction without much external energy. Interestingly, the potential determining step for the TM@GDY SACs (TM = Cr, Fe) is the elementary reaction of $*NO_3 + H^+ + e^- \rightarrow *NO_3H$, while the elementary reaction of $*NO + H^+ + e^- \rightarrow *NOH$ is the potential step for the TM@GDY SACs (TM = V, Mn, Co, Ni, Cu, Ag). Therefore, it is reasonable to conclude that the hydrogenation of the $*NO_x$ species in the NO_3RR process is relatively difficult to occur, leading to more extra energy needed to accelerate the production of NH_3. Moreover, no overt barrier impedes the process from $*NO_3$ to *NO; it is thus reasonably inferred that the electroreduction of

https://doi.org/10.1021/acsomega.2c03588
ACS Omega 2022, 7, 31309−31317

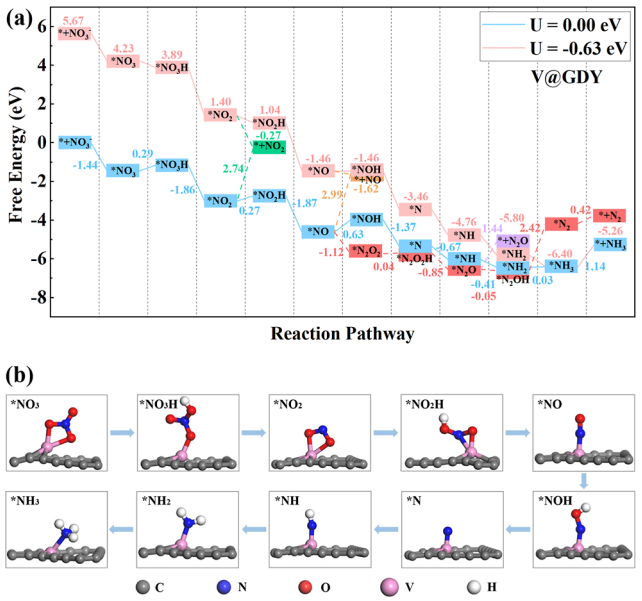

Figure 4. (a) Free energy diagram of the NO_3RR via the N-end pathway on V@GDY at an potential of 0.00 eV and −0.63 eV. The pathways to the release of NO_2, NO, N_2O, and N_2 are also plotted for comparison. (b) Corresponding structures of NO_3RR intermediates (via the N-end pathway) adsorbed on V@GDY.

NO_2^-, NO_2, and NO to produce NH_3 can be realized as well, in agreement with recent experimental results.[11,37]

To inspect the selectivity of the NO_3RR toward NH_3, the possibility of the formation of byproducts (NO_2, NO, N_2O, and N_2) is considered, and the corresponding free energies are also plotted for comparison in the free energy diagram of V@GDY, as shown in Figure 4a. The elementary reaction steps and the corresponding adsorption structures involved the abovementioned byproducts are shown in Figure S7. The energy barriers for the release of NO_2, NO, and N_2O gas reach up to 2.74, 2.99, and 1.44 eV, respectively, on V@GDY, respectively, indicating the considerably difficult formation of these byproducts. Although N_2 shows a lower energy barrier of 0.42 eV for its release, the elementary reaction of $*N_2OH$ to $*N_2$ possesses a high energy barrier of 2.42 eV, which is impeditive for the formation of $*N_2$, much less for the release of N_2. In contrast, the desorption of NH_3 demands less energy of 1.14 eV, which indicates the high selectivity for the NO_3RR toward NH_3 on V@GDY at an electrode potential of 0.00 V. However, with an extra negative electrode potential of −0.63 V applied in the NO_3RR process of V@GDY, we can find that the release of NO_2 and NO gases becomes remarkably accelerated due to much more accumulated free energy caused by the applied electrode potential.[38] Therefore, we can conclude that the desorption process of these byproducts is easier to happen with the applied electrode potential getting more negative, which could lead to the impurity of the NH_3 product. Even so, the details of how the applied electrode potential influences the NO_3RR process need more experimental results to verify the computational conclusions.

The density of states (DOS), band structure, charge and spin density distribution, and charge analysis, are performed to investigate the outstanding catalytic efficiency of V@GDY. The electron density of V@GDY is presented in Figure 5a, where the red regions around the V atom indicate the increasing electron density, which is confirmed by the Bader charge

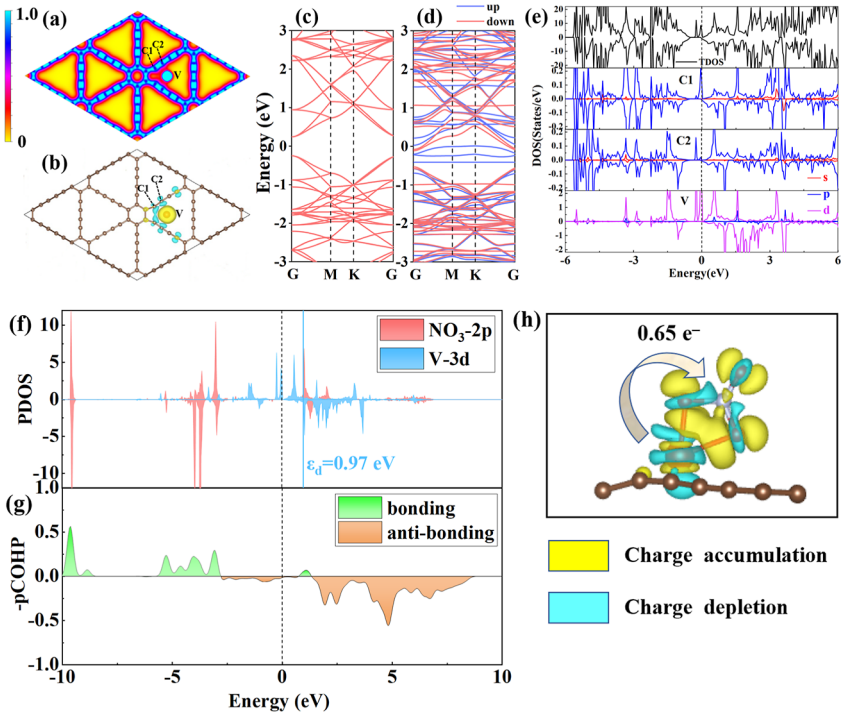

Figure 5. (a) Electron density of the V@GDY with an isosurface of 0.03 e $Bohr^{-3}$. (b) The spin density of the V@GDY with an isosurface of 0.002 e $Bohr^{-3}$. The spin-up and spin-down states are denoted by yellow and blue regions. (c) Band structure of the pristine GDY and (d) V@GDY. (e) DOSof the V@GDY with the Fermi level shifted to 0 eV. (f) Partial DOS (PDOS) and (g) pCOHP of NO_3^- adsorbed on the V@GDY. The dotted lines denote the Fermi level, referring to 0 eV. (h) Charge density difference of NO_3^- adsorbed on the V@GDY with an isosurface of 0.002 e $Bohr^{-3}$.

https://doi.org/10.1021/acsomega.2c03588
ACS Omega 2022, 7, 31309−31317

analysis. The C1 and C2 atoms denoted in Figure 5a,b gain 0.10 e^- and 0.36 e^-, respectively, while the V atom loses 1.10 e^-, serving as an active site. The spin density is primary around the V atom which can be seen in Figure 5b, and the V@GDY monolayer possesses a total spin moment of 2.62 μB. The band structures of the pristine GDY and the V@GDY monolayer are depicted in Figure 5c,d. The pristine GDY possesses a direct bandgap of 0.49 eV, which is nearly consistent with previous theoretical reports.[26] However, the V@GDY displays a metallic character with a magnetic ground state because of the introduction of the occupied d orbital of the V atom, as shown in Figure 5d,e. The intrinsic spin moment could be responsible for the activation of NO_3^- on the V@GDY monolayer and for the high catalytic efficiency, which is in agreement with the conclusion that magnetism within catalysts could improve reaction activity.[39]

To gain further insights into the activation of NO_3^- on V@GDY, the adsorption of NO_3^- on V@GDY can be revealed from two sides. On one hand, the V-3d orbital is almost above the Fermi level (E_F), leading to a positive d-band center (ε_d) of 0.97 eV for V@GDY shown in Figure 5f. Based on previous studies,[40] the positive ε_d value implies the rather strong interaction between the V atom and NO_3^-. On the other hand, the hybridized energy levels of the V-3d orbital and NO_3-2p orbitals split into the bonding and antibonding states, and the adsorption strength is determined by the antibonding states. Namely, the adsorption strength gets weakened when the antibonding population gradually moves down below E_F.[41] The strong adsorption of NO_3^- is thus validated in Figure 5g because only a few antibonding states are below E_F when NO_3^- is adsorbed on V@GDY. Additionally, the charge transfer is observed from the V atom to NO_3^- with 0.65 e^- for V@GDY in Figure 5h, providing powerful clues into the adsorption of NO_3^- as well. Moreover, the Co@GDY with a moderate ΔG_{*NO_3} of −0.13 eV is chosen for further comparison. The left-moving antibonding states shown in Figure S8 and the diminishing charge transfer shown in Figure S9 from the Co atom to NO_3^- on the Co@GDY lead to the weakened NO_3^- adsorption.

As discussed in the former part, the V atom prefers to be anchored at the corner of a triangular ring composed of 18 carbon atoms, leading to the bonding with the C1 and C2 atoms, whose bond length reaches 2.11 Å for the V−C1 bond and 2.07 Å for the V−C2 bond, as shown in Figure 6a. The calculated binding energy (E_b) between the V atom and the GDY monolayer is up to 5.39 eV, resulting from the significant hybridization of V-3d orbitals with C-2p orbitals from the C1 and C2 atoms in the sp hybrid diacetylene chain. Furthermore, the energy difference (ΔE) between the binding energy (E_b) and cohesive energy (E_{coh}) on the V@GDY reaches 0.003 eV, proving the stability of V@GDY. Otherwise, the CI-NEB method is introduced to examine the thermodynamic stability of V@GDY, whose result is demonstrated in Figure 6a−c. The intake of extra energies of 1.40, 1.54, and 1.82 eV is required to transfer the initial state to the corresponding transition state, respectively, showing the excellent thermodynamic stability of V@GDY. Additionally, the AIMD calculations are performed to demonstrate the kinetic stability of the V@GDY monolayer. The total energy oscillates near the initial condition, as shown in Figure 6d, and the geometric structures of V@GDY are preserved well except for a slight distortion in the morphology after 600 K AIMD for 6 ps. It is thus reasonable to conclude

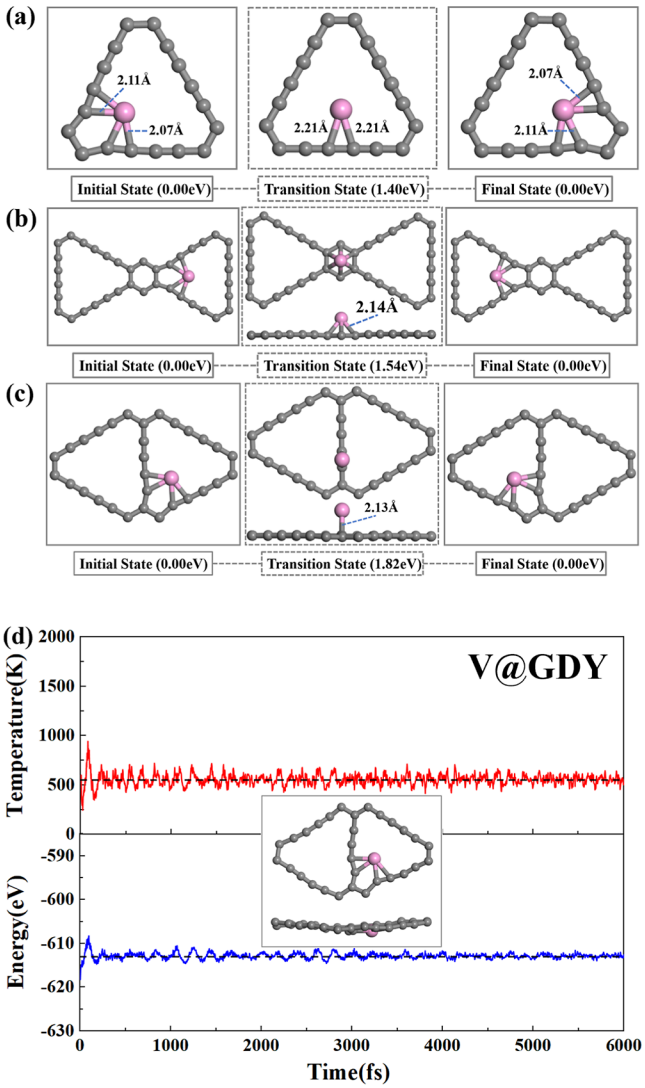

Figure 6. (a) Diffusion pathway of the V atom transferring from the corner to another corner on the same triangular ring. (b) Diffusion pathway of the V atom transferring from a corner to the corner of the opposite triangular ring. (c) Diffusion pathway of the V atom transferring from a corner to the corner of the neighboring triangular ring. The gray and pink balls represent the C atom and V atom, respectively. (d) Energy and temperature evolution vs the AIMD time for the V@GDY and the final structure of V@GDY after AIMD simulation lasting for 6 ps at 600 K.

that the V@GDY can serve as an efficient NO_3RR catalyst for selective ammonia synthesis with high stability.

CONCLUSIONS

In summary, 24 kinds of transition metal atoms (TM = Ti−Cu, Zr−Ag, Hf−Au) are selected to be anchored on the pristine GDY monolayer to construct the NO_3RR SACs. The first-principles calculations are applied to comprehensively investigate the catalytic performance and product selectivity, as well as the structural stability, of these NO_3RR electrocatalysts. Taking the different NO adsorption configurations into consideration, the possible mechanisms of the NO_3RR could be classified as O-end, N-end, O-side, N-side, and NO-dimer pathways. The calculation results denote that the V@GDY shows the lowest limiting potential of −0.63 V versus RHE compared with other TM@GDY SACs (TM = Cr, Mn,

https://doi.org/10.1021/acsomega.2c03588
ACS Omega 2022, 7, 31309−31317

Fe, Co, Ni, Cu, Ag). In terms of selectivity, the NO_3RR process shows a preference for the NH_3 product due to the high energy barriers to the formation of byproducts NO_2, NO, N_2O, and N_2. Meanwhile, the NO_3RR is more likely to happen than the NRR and HER due to the stronger adsorption strength of NO_3^- than the N_2 molecule and H proton on the V@GDY. In addition, the structure of the V@GDY could be retained very well up to 600 K, exhibiting the initial configuration with high thermal stability. Therefore, our theoretical study validates that the V@GDY is a promising electrocatalyst to be fabricated experimentally, which is a new way for nitrate degradation and ammonia synthesis.

COMPUTATIONAL METHODS

All the density functional theory (DFT) calculations were carried out by the Vienna ab initio simulation package (VASP) with the use of Perdew−Burke−Ernzerhof functional within generalized gradient approximation.[42,43] To describe the expansion of the electronic eigenfunctions, the projector-augmented wave method was applied with a kinetic energy cutoff of 520 eV.[44] The DFT-D3 method was adopted for the consideration of describing the van der Waals interactions.[45] The solvation effect was not taken into consideration to simplify the calculation for the fact that the ignorable energy change was witnessed.[46] Bader charge analysis was performed to understand better the charge variation quantitatively.[47] The projected crystal orbital Hamilton population (pCOHP) was calculated by using LOBSTER to analyze the interaction between the TM atom and intermediates.[48] A 2 × 2 × 1 supercell of graphdiyne was accepted, whose vacuum space was 15 Å in the z-direction to minimize interlayer interactions. The Monkhorst-Pack 2 × 2 × 1 *k*-point mesh was employed for the structural optimizations, while the *k*-point mesh was set to 5 × 5 × 1 for the DOS calculations. All atomic positions were fully relaxed until energy and force reached the tolerance of 1×10^{-5} eV and 0.02 eV $Å^{-1}$, respectively. To illustrate the kinetic stability, AIMD simulations were performed with the canonical (*NVT*) ensemble at 600 K for 6 ps.[49] Otherwise, VASPKIT, a convenient and efficient pre-and post-processing program for the VASP code, was used among partial calculations.[50]

The energy difference between the TM@GDY SAC and the single TM atom and pristine GDY is named the binding energy (E_b), which is defined as

$$E_b = E_{TM@GDY} - E_{GDY} - E_{TM}$$

However, the energy difference between an atom of the bulk metal and a single TM atom is stated as the cohesive energy (E_{coh}), which is calculated by

$$E_{coh} = E_{TM-bulk} - E_{TM}$$

The energy difference between E_b and E_{coh}, called ΔE, will be used as a criterion to judge whether the SACs possess thermodynamic stability and is shown as

$$\Delta E = E_b - E_{coh}$$

E_{GDY}, $E_{TM@GDY}$, E_{TM}, and $E_{TM\text{-}bulk}$ mean the energies of pristine GDY, TM@GDY SAC, an isolated TM atom, and a bulk-metal atom, respectively. It is accepted that the TM@GDY SAC can be more favorable to being a SAC if the energy difference (ΔE) is smaller than 0.15 eV, which is suggested by the previous study.[51]

The adsorption energy (E_{ads}) of reaction intermediates on the TM@GDY SAC monolayer is determined by

$$E_{ads} = E_{sum} - E_{adsorbate} - E_{TM@GDY}$$

where E_{sum} denotes the energy of the adsorbate−catalyst system, while $E_{adsorbate}$ denotes the energy of the isolated adsorbate.

According to the computational hydrogen electrode model,[52] the Gibbs free energy change (ΔG) of each elementary step attached to the reaction (NO_3^- to NH_3) is defined as

$$\Delta G = \Delta E + \Delta ZPE - T\Delta S + \Delta U + \Delta pH$$

where ΔE means the adsorption energy obtained from the DFT calculations. ΔZPE denotes the correction of the zero-point energy, while ΔS is the difference of entropy, and T is room temperature (298.15 K), respectively. The calculated ΔZPE and $T\Delta S$ are summarized in Table S6.[34] With the consideration of other external factors, the effect of the applied electrode potential and the pH of the solution are included by the correction of ΔU and ΔpH, respectively. Notably, $\Delta U = U \times e$, where U is the electrode potential, and e is the electron transfer, respectively. $\Delta pH = K_B T \times \ln 10 \times pH$, where K_B is the Boltzmann constant, and pH = 0 in this study.

The first step of the whole reaction is the adsorption of NO_3^- to the TM@GDY SACs, but it is not convenient for the VASP code to calculate the energy of charged NO_3^- directly. So gaseous HNO_3 is chosen as a reference instead to make the calculation feasible to go on with (details in Supporting Information).[53−55] The adsorption energy of NO_3^- (ΔG_{*NO_3}) is described as

$$\Delta G_{*NO_3} = G_{*NO_3} - G_* - G_{HNO_3(g)} + 0.5G_{H_2(g)} + \Delta G_{correct}$$

where G_{*NO_3}, G_*, $G_{HNO_3(g)}$, and $G_{H_2(g)}$ denote the Gibbs free energies of NO_3^- adsorbed on the TM@GDY SACs, TM@GDY substrates, HNO_3 molecules, and H_2 molecules in the gas phase, respectively. $\Delta G_{correct}$ denotes the correction of the adsorption energy which is set to 0.392 eV.[34]

ASSOCIATED CONTENT

Supporting Information

The Supporting Information is available free of charge at https://pubs.acs.org/doi/10.1021/acsomega.2c03588.

The detailed elementary steps of the N-end pathway for the NO_3RR process; the statement of using the energy difference (ΔE) as a criterion for evaluating the stability of the TM@GDY systems; binding energies (E_b) and cohesive energies (E_{coh}) of the TM@GDY SACs; NO_3^-, N_2, and H^+ adsorption Gibbs free energies on the TM@GDY SACs and the corresponding structures; free energy change of each elementary step of the N-end pathway for the NO_3RR process on the TM@GDY SACs; the correction of the zero-point energy and entropy of adsorption species and molecules involved in the NO_3RR process; different NO adsorption configurations on the TM@GDY SACs; splitting structure and desorption structure of $*NO_3H$ and $*NO_2H$ intermediates adsorbed on partial TM@GDY SACs; free energy diagrams of the NO_3RR process via the N-end pathway on the TM@GDY SACs; structures of NO_3RR intermediates (byproducts) adsorbed on the TM@GDY SACs and the elementary reaction steps involved;

https://doi.org/10.1021/acsomega.2c03588
ACS Omega 2022, 7, 31309−31317

PDOS, pCOHP, and charge density differences of NO_3^- adsorbed on the Co@GDY; geometric structure of Ag@GDY after the AIMD simulation lasting for 6 ps at 600 K; and geometric structure of NO_3 adsorbed on the V@GDY after the AIMD simulation lasting for 4.5 ps at 600 K (PDF)

AUTHOR INFORMATION

Corresponding Author

Jike Wang − *The Institute for Advanced Studies, Wuhan University, Wuhan 430072, China;* orcid.org/0000-0001-6711-4465; Email: Jike.Wang@whu.edu.cn

Author

Fei Ai − *The Institute for Advanced Studies, Wuhan University, Wuhan 430072, China*

Complete contact information is available at: https://pubs.acs.org/10.1021/acsomega.2c03588

Notes

The authors declare no competing financial interest.

ACKNOWLEDGMENTS

The numerical calculations in this paper have been done on the supercomputing system in the Supercomputing Center of Wuhan University.

REFERENCES

(1) Smil, V. Detonator of the Population Explosion. *Nature* **1999**, *400*, 415.

(2) Galloway, J. W.; Townsend, A. R.; Erisman, J. W.; Bekunda, M.; Cai, Z. C.; Freney, J. R.; Martinelli, L. A.; Seitzinger, S. P.; Sutton, M. A. Transformation of the Nitrogen Cycle: Recent Trends, Questions, and Potential Solutions. *Science* **2008**, *320*, 889−892.

(3) Kitano, M.; Inoue, Y.; Yamazaki, Y.; Hayashi, F.; Kanbara, S.; Matsuishi, S.; Yokoyama, T.; Kim, S. W.; Hara, M.; Hosono, H. Ammonia Synthesis Using a Stable Electride as an Electron Donor and Reversible Hydrogen Store. *Nat. Chem.* **2012**, *4*, 934−940.

(4) Légaré, M. A.; Chabot, G. B.; Dewhurst, R. D.; Welz, E.; Krummenacher, I.; Engels, B.; Braunschweig, H. Nitrogen Fixation and Reduction at Boron. *Science* **2018**, *359*, 896−900.

(5) Ertl, G. Reactions at Surfaces: From Atoms to Complexity (Nobel Lecture). *Angew. Chem., Int. Ed.* **2008**, *47*, 3524−3535.

(6) Milton, R. D.; Cai, R.; Abdellaoui, S.; Leech, D.; De Lacey, A. L.; Pita, M.; Minteer, S. D. Bioelectrochemical Haber-Bosch Process: An Ammonia-Producing H_2/N_2 Fuel Cell. *Angew. Chem., Int. Ed.* **2017**, *56*, 2680−2683.

(7) van der Ham, C. J.; Koper, M. T.; Hetterscheid, D. G. Challenges in Reduction of Dinitrogen by Proton and Electron Transfer. *Chem. Soc. Rev.* **2014**, *43*, 5183−5191.

(8) Jia, H. P.; Quadrelli, E. A. Mechanistic Aspects of Dinitrogen Cleavage and Hydrogenation to Produce Ammonia in Catalysis and Organometallic Chemistry: Relevance of Metal Hydride Bonds and Dihydrogen. *Chem. Soc. Rev.* **2014**, *43*, 547−564.

(9) Rosca, V.; Duca, M.; de Groot, M. T.; Koper, M. T. M. Nitrogen Cycle Electrocatalysis. *Chem. Rev.* **2009**, *109*, 2209−2244.

(10) Xue, X.; Chen, R.; Yan, C.; Zhao, P.; Hu, Y.; Zhang, W.; Yang, S.; Jin, Z. Review on Photocatalytic and Electrocatalytic Artificial Nitrogen Fixation for Ammonia Synthesis at Mild Conditions: Advances, Challenges and Perspectives. *Nano Res.* **2019**, *12*, 1229−1249.

(11) Choi, J.; Du, H.-L.; Nguyen, C. K.; Suryanto, B. H. R.; Simonov, A. N.; MacFarlane, D. R. Electroreduction of Nitrates, Nitrites, and Gaseous Nitrogen Oxides: A Potential Source of Ammonia in Dinitrogen Reduction Studies. *ACS Energy Lett.* **2020**, *5*, 2095−2097.

(12) Luo, Y.; Li, Q.; Tian, Y.; Liu, Y.; Chu, K. Amorphization Engineered VSe_{2-x} Nanosheets with Abundant Se-Vacancies for Enhanced N_2 Electroreduction. *J. Mater. Chem. A* **2022**, *10*, 1742−1749.

(13) Cai, W.; Han, Y.; Pan, Y.; Zhang, X.; Xu, J.; Zhang, Y.; Sun, Y.; Li, S.; Lai, J.; Wang, L. The Twinned Pd Nanocatalyst Exhibits Sustainable NRR Electrocatalytic Performance by Promoting the Desorption of NH_3. *J. Mater. Chem. A* **2021**, *9*, 13483−13489.

(14) Peng, X.; Liu, H. X.; Zhang, Y.; Huang, Z. Q.; Yang, L.; Jiang, Y.; Wang, X.; Zheng, L.; Chang, C.; Au, C. T.; et al. Highly Efficient Ammonia Synthesis at Low Temperature over a Ru-Co Catalyst with Dual Atomically Dispersed Active Centers. *Chem. Sci.* **2021**, *12*, 7125−7137.

(15) Li, J.; Zhan, G.; Yang, J.; Quan, F.; Mao, C.; Liu, Y.; Wang, B.; Lei, F.; Li, L.; Chan, A. W. M.; et al. Efficient Ammonia Electrosynthesis from Nitrate on Strained Ruthenium Nanoclusters. *J. Am. Chem. Soc.* **2020**, *142*, 7036−7046.

(16) Pang, Y.; Su, C.; Jia, G.; Xu, L.; Shao, Z. Emerging Two-Dimensional Nanomaterials for Electrochemical Nitrogen Reduction. *Chem. Soc. Rev.* **2021**, *50*, 12744−12787.

(17) Seh, Z. W.; Kibsgaard, J.; Dickens, C. F.; Chorkendorff, I.; Nørskov, J. K.; Jaramillo, T. F. Combining Theory and Experiment in Electrocatalysis: Insights into Materials Design. *Science* **2017**, *355*, No. eaad4998.

(18) Duca, M.; Koper, M. T. M. Powering Denitrification: The Perspectives of Electrocatalytic Nitrate Reduction. *Energy Environ. Sci.* **2012**, *5*, 9726−9742.

(19) Lim, J.; Liu, C.-Y.; Park, J.; Liu, Y.-H.; Senftle, T. P.; Lee, S. W.; Hatzell, M. C. Structure Sensitivity of Pd Facets for Enhanced Electrochemical Nitrate Reduction to Ammonia. *ACS Catal.* **2021**, *11*, 7568−7577.

(20) Wang, Y.; Xu, A.; Wang, Z.; Huang, L.; Li, J.; Li, F.; Wicks, J.; Luo, M.; Nam, D. H.; Tan, C. S.; et al. Enhanced Nitrate-to-Ammonia Activity on Copper-Nickel Alloys via Tuning of Intermediate Adsorption. *J. Am. Chem. Soc.* **2020**, *142*, 5702−5708.

(21) Li, L.; Chang, X.; Lin, X.; Zhao, Z. J.; Gong, J. Theoretical Insights into Single-Atom Catalysts. *Chem. Soc. Rev.* **2020**, *49*, 8156−8178.

(22) Gawande, M. B.; Fornasiero, P.; Zbořil, R. Carbon-Based Single-Atom Catalysts for Advanced Applications. *ACS Catal.* **2020**, *10*, 2231−2259.

(23) Lang, R.; Du, X.; Huang, Y.; Jiang, X.; Zhang, Q.; Guo, Y.; Liu, K.; Qiao, B.; Wang, A.; Zhang, T. Single-Atom Catalysts Based on the Metal-Oxide Interaction. *Chem. Rev.* **2020**, *120*, 11986−12043.

(24) Haley, M. M.; Brand, S. C.; Pak, J. J. Carbon Networks Based on Dehydrobenzoannulenes: Synthesis of Graphdiyne Substructures. *Angew. Chem., Int. Ed.* **1997**, *36*, 836−838.

(25) Li, G.; Li, Y.; Liu, H.; Guo, Y.; Li, Y.; Zhu, D. Architecture of Graphdiyne Nanoscale Films. *Chem. Commun.* **2010**, *46*, 3256−3258.

(26) Zhou, J.; Li, J.; Liu, Z.; Zhang, J. Exploring Approaches for the Synthesis of Few-Layered Graphdiyne. *Adv. Mater.* **2019**, *31*, 1803758.

(27) Ma, D. W.; Li, T.; Wang, Q.; Yang, G.; He, C.; Ma, B.; Lu, Z. Graphyne as a Promising Substrate for the Noble-Metal Single-Atom Catalysts. *Carbon* **2015**, *95*, 756−765.

(28) Liu, X.; Tang, W.; Liu, S.; Chen, X.; Li, Y.; Hu, X.; Qiao, L.; Zeng, Y. CO Oxidation on Ni and Cu Embedded Graphdiyne as Efficient Noble Metal-Free Catalysts: A First-Principles Density-Functional Theory Investigation. *Appl. Surf. Sci.* **2021**, *539*, 148287.

(29) Xu, G.; Liu, F.; Lu, Z.; Talib, S. H.; Ma, D.; Yang, Z. Design of Promising Single Rh Atom Catalyst for CO Oxidation Based on Graphdiyne Sheets. *Phys. E* **2021**, *130*, 114676.

(30) Yin, X. P.; Wang, H. J.; Tang, S. F.; Lu, X. L.; Shu, M.; Si, R.; Lu, T. B. Engineering the Coordination Environment of Single-Atom Platinum Anchored on Graphdiyne for Optimizing Electrocatalytic Hydrogen Evolution. *Angew. Chem., Int. Ed.* **2018**, *57*, 9382−9386.

(31) Xue, Y.; Huang, B.; Yi, Y.; Guo, Y.; Zuo, Z.; Li, Y.; Jia, Z.; Liu, H.; Li, Y. Anchoring Zero Valence Single Atoms of Nickel and Iron on Graphdiyne for Hydrogen Evolution. *Nat. Commun.* **2018**, *9*, 1460.

(32) Feng, Z.; Li, R.; Ma, Y.; Li, Y.; Wei, D.; Tang, Y.; Dai, X. Molecule-Level Graphdiyne Coordinated Transition Metals as a New Class of Bifunctional Electrocatalysts for Oxygen Reduction and Oxygen Evolution Reactions. *Phys. Chem. Chem. Phys.* **2019**, *21*, 19651−19659.
(33) Feng, Z.; Tang, Y.; Chen, W.; Li, Y.; Li, R.; Ma, Y.; Dai, X. Graphdiyne Coordinated Transition Metals as Single-Atom Catalysts for Nitrogen Fixation. *Phys. Chem. Chem. Phys.* **2020**, *22*, 9216−9224.
(34) Niu, H.; Zhang, Z.; Wang, X.; Wan, X.; Shao, C.; Guo, Y. Theoretical Insights into the Mechanism of Selective Nitrate-to-Ammonia Electroreduction on Single-Atom Catalysts. *Adv. Funct. Mater.* **2020**, *31*, 2008533.
(35) Wu, J.; Li, J. H.; Yu, Y. X. Theoretical Exploration of Electrochemical Nitrate Reduction Reaction Activities on Transition-Metal-Doped h-BP. *J. Phys. Chem. Lett.* **2021**, *12*, 3968−3975.
(36) Wang, Y.; Wang, C.; Li, M.; Yu, Y.; Zhang, B. Nitrate Electroreduction: Mechanism Insight, in situ Characterization, Performance Evaluation, and Challenges. *Chem. Soc. Rev.* **2021**, *50*, 6720−6733.
(37) Long, J.; Chen, S.; Zhang, Y.; Guo, C.; Fu, X.; Deng, D.; Xiao, J. Direct Electrochemical Ammonia Synthesis from Nitric Oxide. *Angew. Chem., Int. Ed.* **2020**, *59*, 9711−9718.
(38) Qiu, W.; Xie, X. Y.; Qiu, J.; Fang, W. H.; Liang, R.; Ren, X.; Ji, X.; Cui, G.; Asiri, A. M.; Cui, G.; et al. High-Performance Artificial Nitrogen Fixation at Ambient Conditions Using a Metal-Free Electrocatalyst. *Nat. Commun.* **2018**, *9*, 3485.
(39) Li, X. F.; Li, Q. K.; Cheng, J.; Liu, L.; Yan, Q.; Wu, Y.; Zhang, X. H.; Wang, Z. Y.; Qiu, Q.; Luo, Y. Conversion of Dinitrogen to Ammonia by FeN_3-Embedded Graphene. *J. Am. Chem. Soc.* **2016**, *138*, 8706−8709.
(40) Niu, H.; Wang, X.; Shao, C.; Zhang, Z.; Guo, Y. Computational Screening Single-Atom Catalysts Supported on g-CN for N_2 Reduction: High Activity and Selectivity. *ACS Sustainable Chem. Eng.* **2020**, *8*, 13749−13758.
(41) Liu, X.; Jiao, Y.; Zheng, Y.; Jaroniec, M.; Qiao, S. Z. Building Up a Picture of the Electrocatalytic Nitrogen Reduction Activity of Transition Metal Single-Atom Catalysts. *J. Am. Chem. Soc.* **2019**, *141*, 9664−9672.
(42) Perdew, J. P.; Burke, K.; Ernzerhof, M. Generalized Gradient Approximation Made Simple. *Phys. Rev. Lett.* **1996**, *77*, 3865−3868.
(43) Kresse, G.; Furthmüller, J. Efficient Iterative Schemes for Ab Initio Total-Energy Calculations Using a Plane-Wave Basis Set. *Phys. Rev. B: Condens. Matter Mater. Phys.* **1996**, *54*, 11169−11186.
(44) Blöchl, P. E. Projector Augmented-Wave Method. *Phys. Rev. B: Condens. Matter Mater. Phys.* **1994**, *50*, 17953−17979.
(45) Grimme, S. Semiempirical GGA-Type Density Functional Constructed with a Long-Range Dispersion Correction. *J. Comput. Chem.* **2006**, *27*, 1787−1799.
(46) Montoya, J. H.; Tsai, C.; Vojvodic, A.; Nørskov, J. K. The Challenge of Electrochemical Ammonia Synthesis: A New Perspective on the Role of Nitrogen Scaling Relations. *ChemSusChem* **2015**, *8*, 2180−2186.
(47) Tang, W.; Sanville, E.; Henkelman, G. A Grid-Based Bader Analysis Algorithm without Lattice Bias. *J. Phys.: Condens. Matter* **2009**, *21*, 084204.
(48) Nelson, R.; Ertural, C.; George, J.; Deringer, V. L.; Hautier, G.; Dronskowski, R. LOBSTER: Local Orbital Projections, Atomic Charges, and Chemical-Bonding Analysis from Projector-Augmented-Wave-Based Density-Functional Theory. *J. Comput. Chem.* **2020**, *41*, 1931−1940.
(49) Nosé, S. A Unified Formulation of the Constant Temperature Molecular Dynamics Methods. *J. Chem. Phys.* **1984**, *81*, 511.
(50) Wang, V.; Xu, N.; Liu, J.-C.; Tang, G.; Geng, W.-T. VASPKIT: A User-Friendly Interface Facilitating High-Throughput Computing and Analysis Using VASP Code. *Comput. Phys. Commun.* **2021**, *267*, 108033.
(51) Ling, C.; Shi, L.; Ouyang, Y.; Zeng, X. C.; Wang, J. Nanosheet Supported Single-Metal Atom Bifunctional Catalyst for Overall Water Splitting. *Nano Lett.* **2017**, *17*, 5133−5139.
(52) Nørskov, J. K.; Rossmeisl, J.; Logadottir, A.; Lindqvist, L.; Kitchin, J. R.; Bligaard, T.; Jónsson, H. Origin of the Overpotential for Oxygen Reduction at a Fuel-Cell Cathode. *J. Phys. Chem. B* **2004**, *108*, 17886−17892.
(53) Guo, S.; Heck, K.; Kasiraju, S.; Qian, H.; Zhao, Z.; Grabow, L. C.; Miller, J. T.; Wong, M. S. Insights into Nitrate Reduction over Indium-Decorated Palladium Nanoparticle Catalysts. *ACS Catal.* **2017**, *8*, 503−515.
(54) Liu, J.-X.; Richards, D.; Singh, N.; Goldsmith, B. R. Activity and Selectivity Trends in Electrocatalytic Nitrate Reduction on Transition Metals. *ACS Catal.* **2019**, *9*, 7052−7064.
(55) Calle-Vallejo, F.; Huang, M.; Henry, J. B.; Koper, M. T.; Bandarenka, A. S. Theoretical Design and Experimental Implementation of Ag/Au Electrodes for the Electrochemical Reduction of Nitrate. *Phys. Chem. Chem. Phys.* **2013**, *15*, 3196−3202.

https://doi.org/10.1021/acsomega.2c03588
ACS Omega 2022, 7, 31309−31317